

## Rational design of cocatalyst for highly improved ammonia production from photoelectrochemical nitrate reduction

Di Liu<sup>a</sup>, Shuyang Peng<sup>b</sup>, Lulu Qiao<sup>a</sup>, Haoyun Bai<sup>a</sup>, Keyu An<sup>a</sup>, Chunfa Liu<sup>a</sup>, Mingpeng Chen<sup>c</sup>, Kin Ho Lo<sup>b</sup>, Kar Wei Ng<sup>a,d</sup>, Shengjie Peng<sup>e</sup>, Shuangpeng Wang<sup>a,d,\*</sup>, Weng Fai Ip<sup>d,\*\*</sup>, Hui Pan<sup>a,d,\*</sup>

<sup>a</sup> Institute of Applied Physics and Materials Engineering, University of Macau, Macao SAR, China

<sup>b</sup> Department of Electromechanical Engineering, Faculty of Science and Technology, University of Macau, Macao SAR, China

<sup>c</sup> School of Materials and Energy, Yunnan University, New District of Chenggong, Kunming 650000, China

<sup>d</sup> Department of Physics and Chemistry, Faculty of Science and Technology, University of Macau, Macao SAR, China

<sup>e</sup> College of Materials Science and Technology, Nanjing University of Aeronautics and Astronautics, Nanjing 210016, China



### ARTICLE INFO

#### Keywords:

Photoelectrocatalysis  
Nitrate reduction  
Ammonia production  
DFT calculations

### ABSTRACT

Photoelectrochemical nitrate reduction reaction ( $p\text{-NO}_3\text{RR}$ ) has been one of the most promising ways for ambient ammonia synthesis. However, current trials haven't realized efficient ammonia production due to low ammonia yield. Herein, we present that silicon (Si) photocathode with CoNi as co-catalyst can achieve low onset potential, high ammonia yield, and close-to-unity selectivity in  $p\text{-NO}_3\text{RR}$ . The optimal photocathode ( $\text{Co}_{0.95}\text{Ni}_{0.05}/\text{Si}$ ) exhibits a record-high ammonia yield of  $2054 \mu\text{g h}^{-1} \text{cm}^{-2}$  with an excellent Faraday efficiency (FE) of 98.6% at only  $-0.1 \text{ V}$  vs. reversible hydrogen electrode (RHE), which outperforms reported photocathodes in literature. Our characterizations and calculations demonstrate that the metallic Co dominantly exists as the interior of  $\text{Co}_{0.95}\text{Ni}_{0.05}/\text{Si}$  that accelerates electron transfer, while Ni is introduced into  $\text{Co}_3\text{O}_4$  on the surface that optimizes the adsorption behavior and improves the activity and selectivity. We believe that the findings provide insightful guidance for enhanced performance towards large-scale ammonia synthesis by photoelectrochemical nitrate reduction.

### 1. Introduction

Carbon neutrality has been an international mission for most countries [1-4]. Reducing carbon emissions is one of the important parts of the mission by alleviating our dependence on fossil fuels [5-8]. It has been the biggest challenge for us to find alternative ways toward sustainable development, which is desired by industries [9,10]. The industry for ammonia ( $\text{NH}_3$ ) production consumes 2–3% of the world's natural gas production yearly (1–2% of the world's energy supply) and releases huge amounts of greenhouse gases [11-14]. However, our human society has to keep the production rate increasing because ammonia as the fertilizer is dominantly important to maintain the crop yield for the increasing population. At the same time, ammonia is one of the most important chemicals, which has been widely used in various industries. Hence, it is urgent to find a green way for ammonia production that has little dependence on fossil fuels [15,16].

In this regard, catalytic ammonia synthesis has been considered as one of the most promising ways, which can be performed under mild environments and operated by green energy [17]. Among the reported catalytic ammonia production systems [18-22], nitrate reduction reaction ( $\text{NO}_3\text{RR}$ ), including electrocatalytic and photoelectrochemical (PEC)  $\text{NO}_3\text{RR}$  ( $e\text{-NO}_3\text{RR}$  and  $p\text{-NO}_3\text{RR}$ ), has attracted growing attention because it can not only generate value-added ammonia, but remove the harmful nitrate ions at the same time [23-25]. The  $e\text{-NO}_3\text{RR}$  process can have a high ammonia yield and be easily operated [26-28]. However, the practical application of efficient ammonia production is limited due to the requirement of a high potential, particularly in neutral environments where  $\text{NO}_3^-$ -containing wastewater is present [29-31,5]. Therefore, photoelectrochemical nitrate reduction, which can reduce the onset potential, has been considered as one of the most promising ways [32,33]. However, the PEC performance needs to be improved dramatically due to the low ammonia yield rate [34-37], where both the

\* Corresponding authors at: Institute of Applied Physics and Materials Engineering, University of Macau, Macao SAR, China.

\*\* Corresponding author.

E-mail addresses: [spwang@um.edu.mo](mailto:spwang@um.edu.mo) (S. Wang), [andyip@um.edu.mo](mailto:andyip@um.edu.mo) (W.F. Ip), [huipan@um.edu.mo](mailto:huipan@um.edu.mo) (H. Pan).

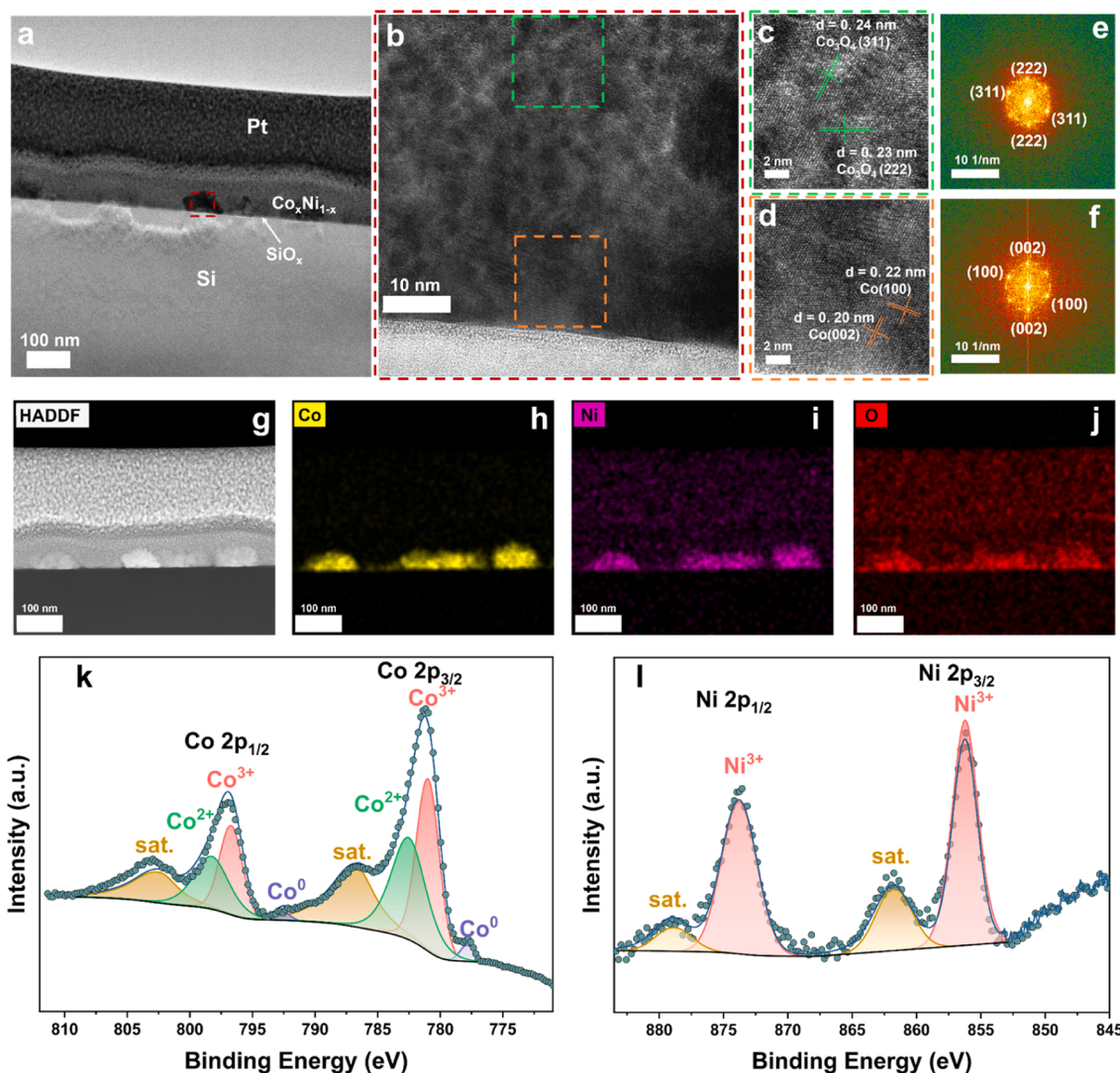


**Fig. 1.** Co<sub>0.95</sub>Ni<sub>0.05</sub>/Si photocathode: (a) TEM image, (b), (c) & (d) HR-TEM images, (e) & (f) FFT images, (g) HAADF-STEM image, and the elemental EDX mappings for (h) Co, (i) Ni, and (j) O. (k) Co 2p and (l) Ni 2p XPS spectra.

photocurrent and ammonia selectivity have to be considered. For the photocurrent density, the high photovoltage and fast reaction kinetics are the key challenges [38]. Silicon (Si) with high reservation, mature fabrication, efficient absorption coefficient, and suitable bandgap has been recognized as the most promising solar-harvesting substrate for industrial applications [39-41]. Importantly, the metal-insulator-semiconductor (MIS) structure has been reported to be an effective way to improve the photovoltage and photocurrent density in the PEC process because of built-in electric field [42-44], where the metal can work as co-catalyst at the same time. Though Kim et al. successfully applied the structure and realized a high ammonia selectivity of 95.6% [32], they only achieved a low ammonia yield of 7.07  $\mu\text{g h}^{-1}$   $\text{cm}^{-2}$  due to the low reaction activity of Au as co-catalysts. Therefore, the design of co-catalysts is necessary for the applications of PEC nitrate reduction.

In this work, we fabricated a series of Co<sub>x</sub>Ni<sub>1-x</sub>/Si photocathodes by photo-assisted electrodeposition of CoNi with different Co-Ni ratios onto commercial Si wafers, and evaluated their p-NO<sub>3</sub>RR performances. Our photocathode can obtain a high onset potential of 0.42 V vs. RHE. Importantly, the photocathode with the optimal co-catalyst achieves a high ammonia yield rate of 485  $\mu\text{g h}^{-1}$   $\text{cm}^{-2}$  and excellent Faraday efficiency (FE) of 98.4% at only 0.2 V vs. RHE, which are much superior to

those of reported p-NO<sub>3</sub>RR photocathodes.

## 2. Experimental methods

### 2.1. Synthesis of Co<sub>x</sub>Ni<sub>1-x</sub>/Si photoanode

The Co<sub>x</sub>Ni<sub>1-x</sub>/Si photoanode was fabricated on a (100) p-type Si substrate by using a simple photo-assisted electrodeposition strategy (Figure S1). Firstly, a piece of p-type Si (5 mm \* 5 mm \* 0.5 mm) with (100) facet was ultrasonically cleaned by acetone, ethanol, and deionized (DI) water several times. Subsequently, the Si substrate was immersed in 5 wt% hydrofluoric acid for 3 mins to remove the native SiO<sub>x</sub> layer and reduce contact resistance. Then, the back electrode and protection layer were fabricated by a general method as in our previous work [39].

For the photo-assisted electrodeposition process, the classic 3-electrode system was assembled, where the treated Si was the working electrode, the Pt tablet was adopted as the counter electrode, the SCE electrode was utilized as the reference electrode to record the stability during deposition, and a simulated sunlight with an illumination power density of 100 mW  $\text{cm}^{-2}$  is applied for assistance (Figure S1). Additionally, a series of solutions consisting of 3x mmol Co(NO<sub>3</sub>)<sub>2</sub>·4 H<sub>2</sub>O, 3

(1-x) mM  $\text{Ni}(\text{NO}_3)_2 \cdot 4 \text{ H}_2\text{O}$ , 6 mmol  $\text{H}_3\text{BO}_3$ , and 60 ml DI water were utilized as electrolyte for the electrodeposition of  $\text{Co}_x\text{Ni}_{1-x}$  on Si. The electrodeposition process was conducted for 2 s under  $-4 \text{ mA} \cdot \text{cm}^{-2}$ .

## 2.2. Characterizations

A Zeiss Sigma instrument was adopted to obtain field emission scanning electron microscopy (SEM) at an acceleration voltage of 3 kV. The focused ion beam (FIB, Zeiss Sigma) technique was utilized for preparing the cross-sectional TEM sample. A Tecnai G2F30 system was used for acquiring high-resolution transmission electron microscopy (HR-TEM) and energy-dispersive X-ray spectra (EDX) at an acceleration voltage of 200 kV. The surface states and work functions of photocathodes were analyzed by X-ray photoelectron spectroscopy (XPS) and Ultraviolet photoelectron spectroscopy, respectively, on a Thermo Fisher Scientific Theta Probe with Mg Ka ( $\hbar \nu = 1253.6 \text{ eV}$ ) as the excitation source. The roughness of the surface was measured by an atomic force microscope (AFM, Veeco 3100 SPM). All Ultraviolet-visible (UV-Vis) absorption spectra experiments were implemented on the Shimadzu UV-2600 spectrophotometer (Tokyo, Japan). The working electrode area was  $0.25 \text{ cm}^2$ . The H Nuclear Magnetic Resonance Spectra (1 H NMR) was employed for the quantification of  $^{14}\text{NH}_4^+$  and  $^{15}\text{NH}_4^+$ . where potassium-15nitrate ( $\text{K}^{15}\text{NO}_3$ , 99 atom %) was employed as the nitrogen source for isotope-labeled nitrate reduction experiments to trace the origin of the produced ammonia. The electrolyte solution consisted of 1 M potassium hydroxide (KOH) mixed with 0.1 M  $\text{K}^{14}\text{NO}_3/\text{K}^{15}\text{NO}_3$ . Following the p-NO<sub>3</sub>RR at  $-0.6 \text{ V}$  vs. RHE, the electrolyte containing the generated  $^{14}\text{NH}_4^+$  and  $^{15}\text{NH}_4^+$  was extracted and its pH was adjusted to approximately 2 using 1 M hydrochloric acid (HCl). This prepared solution was then quantified using 1 H NMR at 300 MHz, employing a solvent composition of 90% by volume  $\text{H}_2\text{O}$  and 10% by volume DMSO, with maleic acid serving as the internal standard.

## 2.3. Photoelectrochemical measurements

The photoelectrochemical performance of the photocathode was evaluated by a ModuLab XM workstation at ambient conditions. A H-type electrochemical cell equipped with three electrodes and a Celgard 2500 membrane as a separator was applied. The counter electrode was a platinum plate, the reference electrode was Ag/AgCl (saturated KCl), and the working electrode was as-prepared  $\text{Co}_x\text{Ni}_{1-x}/\text{Si}$  photocathodes (the geometric area:  $0.5 \text{ cm} \times 0.5 \text{ cm}$ ). 0.25 M  $\text{K}_2\text{B}_4\text{O}_7$  (pH=9.5) was used as the electrolyte. The membrane was fully washed with DI water prior to use. To simulate sunlight ( $100 \text{ mW} \cdot \text{cm}^{-2}$ ), the solar simulator was employed (AM 1.5 G, ABET TECHNOLOGIES). The two compartments of H-cell were filled with 25 ml solution (0.25 M  $\text{K}_2\text{B}_4\text{O}_7 + 0.1 \text{ M KNO}_3$ ) and then degassed by Ar (99.999%) for more than 30 mins. The polarization curves were recorded by linear sweep voltammetry (LSV) at a scan rate of  $10 \text{ mV s}^{-1}$  without iR correction from 0 to  $-1.5 \text{ V}$  vs. Ag/AgCl. Furthermore, the chronoamperometry (i-t) was performed under various potentials for 1 hour to investigate the FE and yield rate of ammonia. The current density was calculated by normalizing with the geometric area of the working electrode. All recorded electrode potentials vs. Ag/AgCl were transformed to potentials against RHE according to  $E_{\text{RHE}} = E_{\text{Ag/AgCl}} + 0.197 + 0.0591 \times \text{pH}$ . Electrochemical impedance spectroscopy (EIS) was recorded in a frequency range of 10 kHz to 0.01 Hz at 0 V vs. RHE. The electrochemically active surface area (ECSA) was estimated by measuring the double-layer capacitance ( $C_{dl}$ ) via the cyclic voltammetry (CV) test at the scan rates of  $40\text{--}100 \text{ mV s}^{-1}$ . The Suncat band-pass filters were utilized for the measurement of photocurrent under monochromatic light with various wavelengths, where the photocurrent is obtained by the differences of current densities measured under dark and the filtered light.

## 3. Results

### 3.1. Structural characterizations

The transmission electron microscope (TEM) images reveal that the fabricated photocathodes consist of Si,  $\text{Co}_x\text{Ni}_{1-x}$ , and  $\text{SiO}_x$  from the natural oxidation of Si (Fig. 1a, b & S2), which is a typical metal/insulator/semiconductor interface, where the middle insulating  $\text{SiO}_x$  layer could reduce the pinning of surface states and thus enhance the photo-voltage. Additionally,  $\text{Co}_{0.95}\text{Ni}_{0.05}$  is found to be composed of nanoparticles with a diameter of about 100 nm, which are uniformly distributed on Si (Fig. 1a). The high-resolution TEM (HR-TEM) images and corresponding fast Fourier transfer (FFT) show that the inner parts of  $\text{Co}_{0.95}\text{Ni}_{0.05}$  nanoparticles have the lattice spacings of 0.20 and 0.22 nm, which match well with the (100) and (002) facets of metallic Co, respectively (Fig. 1d & f). In contrast, there is an obvious oxide layer on the nanoparticle's surface, where the lattice fringes correspond to the (311) and (222) facets of spinel  $\text{Co}_3\text{O}_4$ , respectively (Fig. 1c & e). Therefore, the deposited co-catalyst is composed of Co-based alloys (inner) and corresponding metal oxides (surface). Except for Pt (the protective layer during the focused-ion-beam process), the energy-dispersed X-ray spectroscopy (EDX) mappings confirm the existence of Co, Ni, O, and Si elements (Fig. 1g-j & S2, Table S1). The elemental distribution further testifies the MIS structure (Fig. 1j & S2c). Furthermore, the EDX results also illustrate the even distribution of Ni element (Fig. 1i), demonstrating the successful incorporation of Ni into metallic Co or spinel  $\text{Co}_3\text{O}_4$ . For further understanding of the as-synthesized catalysts, the X-ray photoelectron spectroscopy (XPS) spectra were analyzed to uncover the composition and valence information. The high-resolution Co 2p spectrum of  $\text{Co}_{0.95}\text{Ni}_{0.05}/\text{Si}$  shows eight main peaks, which include the  $2p_{3/2}$  and  $2p_{1/2}$  peaks of  $\text{Co}^{2+}$ ,  $\text{Co}^{3+}$ ,  $\text{Co}^0$  and their satellite peaks (Fig. 1k). More specifically, Co mainly exists as +2 and +3, illustrating the spinel  $\text{Co}_3\text{O}_4$  on the surface, consistent with the aforementioned results. Additionally, the Co 2p spectrum also reveals the existence of inner  $\text{Co}^0$  with low peak intensity. In contrast, only  $2p_{3/2}$ ,  $2p_{1/2}$  and their satellite peaks of  $\text{Ni}^{3+}$  can be observed in the Ni 2p spectrum of  $\text{Co}_{0.95}\text{Ni}_{0.05}/\text{Si}$ , indicating that Ni is incorporated into spinel  $\text{Co}_3\text{O}_4$  (Fig. 1l). The existence of  $\text{Ni}^0$  cannot be observed in Co-rich samples ( $\text{Co}_{0.95}\text{Ni}_{0.05}/\text{Si}$ ,  $\text{Co}_{0.75}\text{Ni}_{0.25}/\text{Si}$ , and  $\text{Co}_{0.50}\text{Ni}_{0.50}/\text{Si}$ ) (Figures S3 & S4), because the Ni deposition is limited [45] and Co is deposited in preference to Ni [46]. Therefore, the metallic  $\text{Co}^0$  is dominantly existed in the inner part of the nanoparticles in the Co-rich samples, while Ni is coexisted with Co on the surface, which is naturally oxidized to Ni-incorporated  $\text{Co}_3\text{O}_4$  ( $\text{Ni-Co}_3\text{O}_4$ ). For  $\text{Co}_{0.25}\text{Ni}_{0.75}/\text{Si}$ , the metallic  $\text{Ni}^0$  and  $\text{Co}^0$  are both found, demonstrating the priority of Co deposition during the preparation (Figures S3 & S4). In addition, the O 1 s spectra of  $\text{Co}_{0.95}\text{Ni}_{0.05}/\text{Si}$  are mainly contributed by the oxygen vacancies ( $\sim 531.5 \text{ eV}$ ) of crystalline  $\text{Ni-Co}_3\text{O}_4$  and  $\text{SiO}_x$  (Figure S5) [47].

A series of characterizations were carried out to illustrate the surface morphology of as-fabricated photocathodes. The scanning electron microscope (SEM) images (Figures S6-S8) show that Co/Si,  $\text{Co}_{0.95}\text{Ni}_{0.05}/\text{Si}$ , and other photocathodes are composed of nanoparticles decorated on the Si substrates. We see that the size and density of nanoparticles are varied on different photocathodes. For example, the particle size of  $\text{Co}_{0.95}\text{Ni}_{0.05}/\text{Si}$  is smaller than that of Co/Si, while the distribution density is higher than that of Co/Si (Figure S6), revealing that the Ni incorporation could reduce the particle size, and increase the distribution density. The atomic force microscope (AFM) images of Co/Si and  $\text{Co}_{0.95}\text{Ni}_{0.05}/\text{Si}$  further confirm the morphology of nanoparticles on the substrate. We see that the roughness of  $\text{Co}_{0.95}\text{Ni}_{0.05}/\text{Si}$  is lower than that of Co/Si, revealing the smaller size, consistent with the SEM images (Figure S6).

### 3.2. Photoelectrochemical performances

The linear sweep voltammetry (LSV) curves show that all the  $\text{Co}_x\text{Ni}_{1-x}$

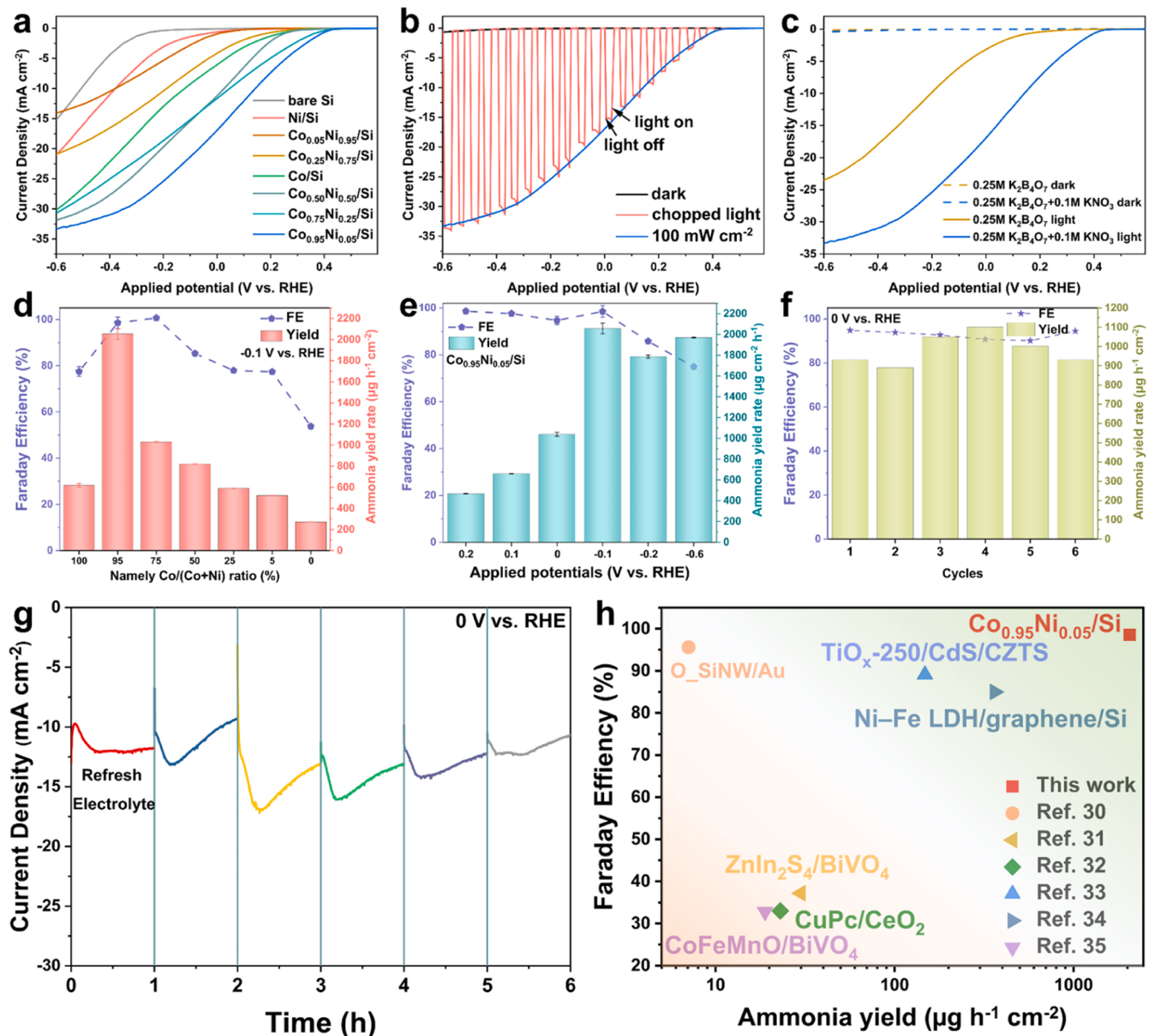


**Fig. 2.** Photoelectrochemical performances of  $\text{Co}_x\text{Ni}_{1-x}/\text{Si}$ . (a) LSV curves of  $\text{Co}_x\text{Ni}_{1-x}/\text{Si}$ ; (b) photo-response of  $\text{Co}_{0.95}\text{Ni}_{0.05}/\text{Si}$  in the  $0.25 \text{ M } \text{K}_2\text{B}_4\text{O}_7 + 0.1 \text{ M } \text{KNO}_3$  solution under chopped light, (c) LSV curves of  $\text{Co}_{0.95}\text{Ni}_{0.05}/\text{Si}$  in the  $0.25 \text{ M } \text{K}_2\text{B}_4\text{O}_7 + 0.1 \text{ M } \text{KNO}_3$  and  $0.25 \text{ M } \text{K}_2\text{B}_4\text{O}_7$ , (d) ammonia yields and FE for  $\text{Co}_x\text{Ni}_{1-x}/\text{Si}$  under  $-0.1 \text{ V}$  vs. RHE, (e) ammonia yields and FE for  $\text{Co}_{0.95}\text{Ni}_{0.05}/\text{Si}$  photocathode under different applied potentials, (f) ammonia yields and FE for  $\text{Co}_{0.95}\text{Ni}_{0.05}/\text{Si}$  during the durability test, (g) I-t curves of  $\text{Co}_{0.95}\text{Ni}_{0.05}/\text{Si}$ , and (h) the comparison of ammonia yields and FE of photocathodes.

$\text{x}/\text{Si}$  photocathodes exhibit obvious photocurrent under light illumination (Fig. 2a). In addition, the positive onset potentials are observed for  $\text{Co}_x\text{Ni}_{1-x}/\text{Si}$  photocathodes if the Co-Ni ratios are higher than 25%. Specifically, the onset potential of  $\text{Co}_{0.95}\text{Ni}_{0.05}/\text{Si}$  reaches  $0.42 \text{ V}$  vs. RHE, which is much superior to those of other photocathodes and bare Si (Fig. 2a), illustrating the loaded co-catalysts reduce the  $\text{NO}_3\text{RR}$  overpotential dramatically. Furthermore,  $\text{Co}_{0.95}\text{Ni}_{0.05}/\text{Si}$  shows an obvious light response under the chopped light (Fig. 2b), confirming that the excellent  $\text{NO}_3\text{RR}$  performance is induced by external light. To illustrate the wavelength-dependent performance of  $\text{Co}_{0.95}\text{Ni}_{0.05}/\text{Si}$ , we carried out the incident monochromatic photon-electron conversion efficiency (IPCE) measurement by band-pass filter under  $-0.6 \text{ V}$  (Figure S10), which indicates that the  $\text{Co}_{0.95}\text{Ni}_{0.05}/\text{Si}$  photocathode shows obvious light responses under all the test wavelengths ( $450 \text{ nm} - 900 \text{ nm}$ ) with the highest IPCE value of 31.09%. Furthermore,  $\text{Co}_{0.95}\text{Ni}_{0.05}/\text{Si}$  exhibits an obvious low current density in  $0.25 \text{ M } \text{K}_2\text{B}_4\text{O}_7$  than that in  $0.25 \text{ M } \text{K}_2\text{B}_4\text{O}_7 + 0.1 \text{ M } \text{KNO}_3$  (Fig. 2c), which illustrates its excellent

performance for p- $\text{NO}_3\text{RR}$ . The chronoamperometry tests under  $0 \text{ V}$  vs. RHE show that all photocathodes have prominent ammonia selectivity with an FE of more than 90% (Figures S9, S13-S16). Moreover,  $\text{Co}_{0.95}\text{Ni}_{0.05}/\text{Si}$  exhibits superior selectivity with a high ammonia FE ( $> 90\%$ ) that can be maintained under a wide range of  $0.2 \text{ V}$  to  $-0.1 \text{ V}$ . In contrast, the ammonia FE of  $\text{Co}/\text{Si}$  and Ni-rich samples (including  $\text{Co}_{0.5}\text{Ni}_{0.5}/\text{Si}$ ,  $\text{Co}_{0.25}\text{Ni}_{0.75}/\text{Si}$ , and  $\text{Co}_{0.05}\text{Ni}_{0.95}/\text{Si}$ ) sharply decrease under high potentials, because of the competition from HER and the formation of by-products (Figures S13-S16).  $\text{Co}_{0.95}\text{Ni}_{0.05}/\text{Si}$  exhibits the highest ammonia yield among the tested samples under different applied potentials, which agrees well with the LSV curves (Fig. 2a & 2d). Especially,  $\text{Co}_{0.95}\text{Ni}_{0.05}/\text{Si}$  shows the highest ammonia yield of  $2054 \mu\text{g h}^{-1} \text{cm}^{-2}$  with a superior FE of 98.6% (Fig. 2e) under  $-0.1 \text{ V}$  vs. RHE, which exceeds all reported p- $\text{NO}_3\text{RR}$  photocathodes to date (Fig. 2h) [32-37]. Additionally, the  $\text{Co}_{0.95}\text{Ni}_{0.05}/\text{Si}$  photocathode even shows a remarkable ammonia yield of  $467 \mu\text{g h}^{-1} \text{cm}^{-2}$  with an FE of 98.4% at only  $0.2 \text{ V}$  vs. RHE due to the superior onset potential (Fig. 2e).

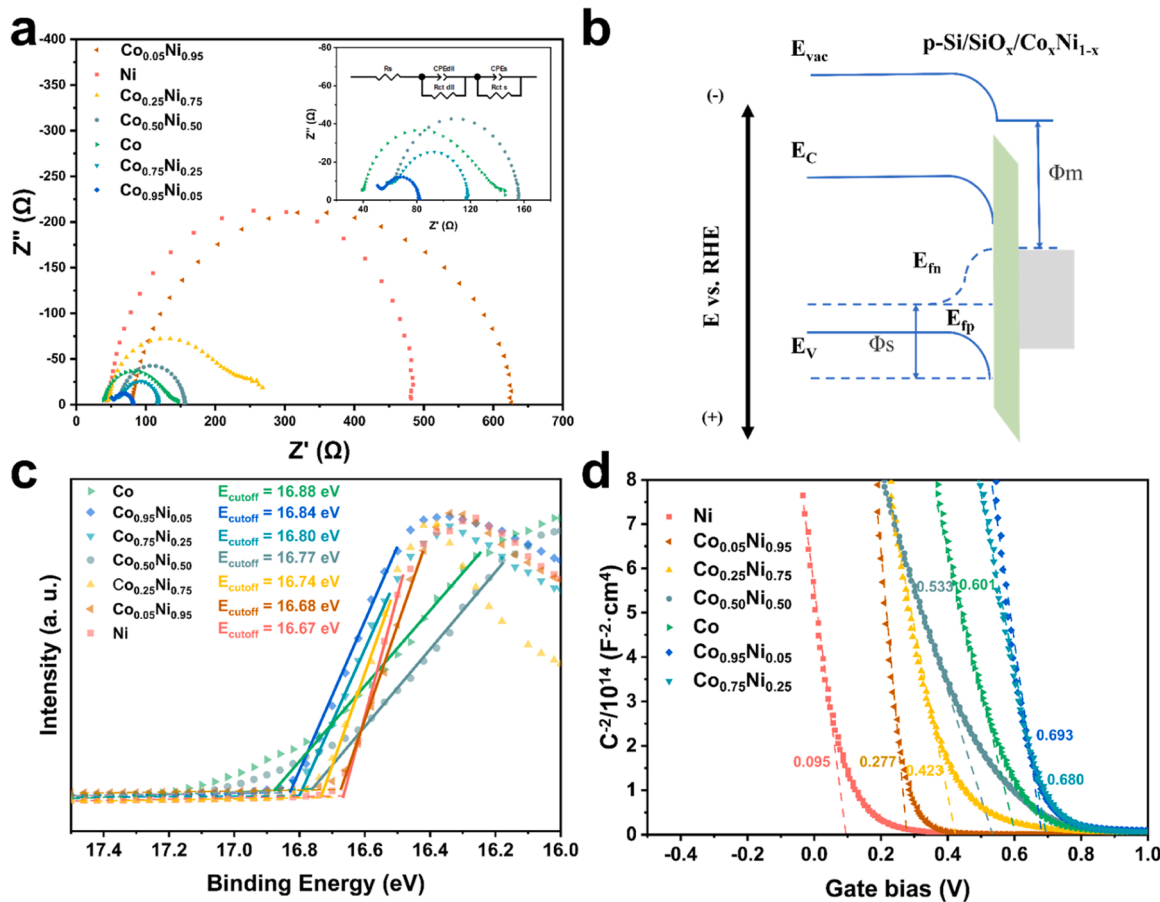


**Fig. 3.** (a) The EIS spectra of  $\text{Co}_x\text{Ni}_{1-x}/\text{Si}$  photocathodes under 100 mW light at 0 V vs. RHE. (b) Schematic diagram for the energy band structure of  $\text{Co}_x\text{Ni}_{1-x}/\text{Si}$ . (c) The UPS results of  $\text{Co}_x\text{Ni}_{1-x}/\text{Si}$  photocathodes. (d) The Mott-Schottky (MS) curves of  $\text{Co}_x\text{Ni}_{1-x}/\text{Si}$  photocathodes in the dark.

However, the FE starts to decrease when the applied potential arrives  $-0.2$  V due to the severe competition from HER, leading to the lower ammonia yield under  $-0.6$  V than that under  $-0.1$  V (Fig. 2e). Importantly,  $\text{Co}_{0.95}\text{Ni}_{0.05}/\text{Si}$  shows high stability (Fig. 2g). Although the current density of  $\text{Co}_{0.95}\text{Ni}_{0.05}/\text{Si}$  varies during each test, it almost recovers to the initial state when the electrolyte is refreshed, illustrating robust durability. In addition, the high ammonia FE ( $> 90\%$ ) and corresponding average ammonia yield ( $\sim 900 \mu\text{g h}^{-1} \text{cm}^{-2}$ ) are sustained during the stability test (Fig. 2f). A slight decrease in current density is observed after the 6 cycles because the particles become bigger and sparser (Figure S7). Furthermore, we also carried out another 20 h stability test under 0 V vs. RHE on  $\text{Co}_{0.95}\text{Ni}_{0.05}/\text{Si}$  photocathode without refreshing the electrolyte. The current density was maintained during this test, which further demonstrates the superior durability (Figure S11). Moreover, the spectroscopic analysis shows that the peak patterns for generated ammonia are various when the nitrogen source are  $^{14}\text{NO}_3^-$  and  $^{15}\text{NO}_3^-$ , respectively, which indicates the detected  $\text{NH}_3$  is originated from the p- $\text{NO}_3\text{RR}$  (Figure S12). The XPS spectra of  $\text{Co}_{0.95}\text{Ni}_{0.05}/\text{Si}$  after the stability test (Figure S17) show that the Co 2p, Ni 2p, and O 1s spectra have no obvious change, demonstrating that the oxides phase is kept without the surface reconstruction to  $\text{Co}(\text{OH})_2$  during the process, which is different from  $\text{Ni}-\text{Co}_3\text{O}_4$  in the electrochemical nitrate reduction [48]. During the e- $\text{NO}_3\text{RR}$  process, the surface reconstruction is closely related to the applied potential [49]. Hence, the low applied potential may not trigger the surface reconstruction, which contributes to the excellent stability of  $\text{Co}_{0.95}\text{Ni}_{0.05}/\text{Si}$ . However, a small peak assigned to the lattice oxygens appears on the O1s spectrum of  $\text{Co}_{0.95}\text{Ni}_{0.05}/\text{Si}$  ( $\sim 529.1$  eV) after the durability test, which might be induced by the decrease of surface oxygen vacancies due

to the movement of nanoparticles.

### 3.3. Kinetics and band alignment

To unravel the origin of enhanced PEC performance, a series of characterizations were carried out (Fig. 3). The electrochemical impedance spectroscopy (EIS) spectra show that  $\text{Co}_{0.95}\text{Ni}_{0.05}/\text{Si}$  possesses the lowest  $R_{ct}$  value under 0 V vs. RHE (Fig. 3a, Table S2), confirming the fastest reaction kinetics, consistent with the lowest onset potential and Tafel slope (Figure S18). In the MIS structure, the reaction kinetics are greatly affected by the charge carrier dynamics (Fig. 3b), which is determined by the energy band alignment between the loaded metal and p-type Si (p-Si). For balancing the Fermi level of p-Si and the loaded metal, the conduction and valence bands of p-Si shall bend upwards to form an energy barrier for prohibiting the hole transmission, resulting in a built-in electric field that accelerates the electron transfer from p-Si to co-catalyst (Fig. 3b) [50]. Therefore, the photovoltage is positively correlated with the energy barrier, as determined by the band alignment [51]. More specifically, the energy barrier is affected by the energy difference of Fermi level between p-Si and the loaded metal, and the flat band voltage ( $V_{fb}$ ), which is determined by the contact between the photocathode and electrolyte [52]. The ultraviolet photoelectron spectroscopy (UPS) results show that the work function of the loaded metal is decreased with the increase of the Co-Ni ratio (Fig. 3c), in consistency with the XPS results (Fig. 1, S3, & S4). The low work function implies the shallow Fermi level, which shall increase the Schottky barrier and thus improve the photovoltage [53]. Hence, the photovoltages of Co-rich photocathodes are higher than those of Ni-rich photocathodes. Furthermore, the Mott-Schottky (MS) plots of these

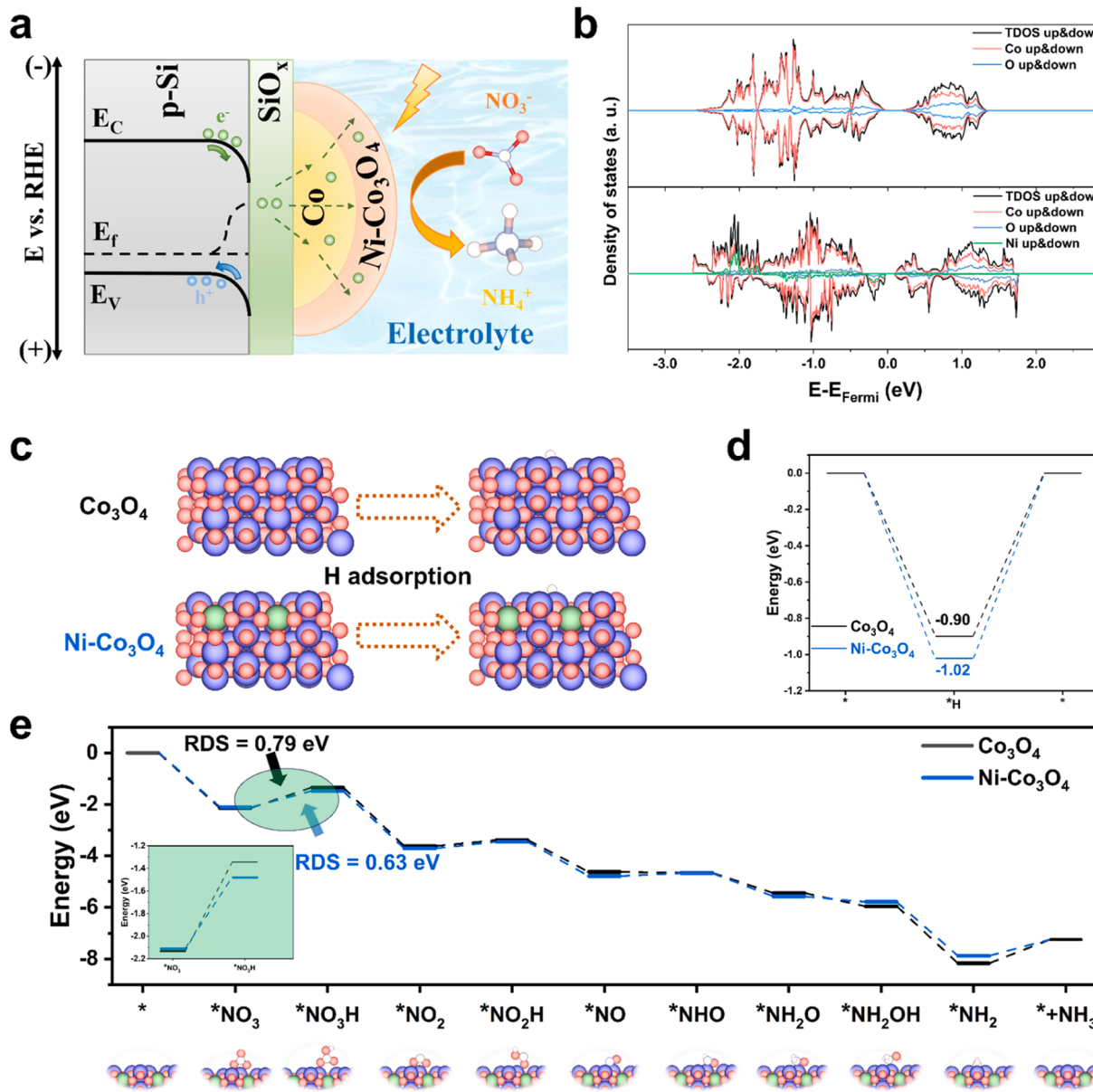


**Fig. 4.** (a) The schematic structure of Co<sub>0.95</sub>Ni<sub>0.05</sub>/Si; (b) the DOSs of Co<sub>3</sub>O<sub>4</sub> and Ni-Co<sub>3</sub>O<sub>4</sub>; (c) The side view of clean and hydrogen-adsorbed (311) Co<sub>3</sub>O<sub>4</sub> and Ni-Co<sub>3</sub>O<sub>4</sub> surface; The energy profiles for HER (d) and NO<sub>3</sub>RR (e) on Co<sub>3</sub>O<sub>4</sub> and Ni-Co<sub>3</sub>O<sub>4</sub>.

photocathodes were characterized for estimating the V<sub>fb</sub> values (Fig. 3d). We see that Co<sub>0.95</sub>Ni<sub>0.05</sub>/Si and Co<sub>0.75</sub>Ni<sub>0.25</sub>/Si possess the highest V<sub>fb</sub> values, which are consistent with the high photovoltages and corresponding low onset potentials. In summary, Co<sub>0.95</sub>Ni<sub>0.05</sub>/Si shows higher photovoltage and photocurrent density than other photocathodes because of the enhanced separation of carriers and charge transfer, fast reaction kinetics, and abundant active sites for the NO<sub>3</sub>RR process (Figure S19).

#### 3.4. DFT calculations

Based on the characterizations, the structure of Co<sub>0.95</sub>Ni<sub>0.05</sub>/Si can be schematically expressed as p-Si/SiO<sub>x</sub>/Co/Ni-Co<sub>3</sub>O<sub>4</sub> (Fig. 4a). Thus, the improvement in the reaction kinetics and ammonia selectivity is strongly correlated with the Ni-Co<sub>3</sub>O<sub>4</sub> surface. Theoretic calculations were carried out based on density-functional theory (DFT) to reveal the underlying mechanism of the reaction kinetics and improved selectivity. Our calculations show that Co in the CoO<sub>4</sub> tetrahedron is easier to be

replaced by Ni than that in the CoO<sub>6</sub> octahedron because of lower formation energy (Figure S20). The calculated densities of states (DOSS) (Fig. 4b) show the Ni-incorporation introduces the defect energy level, which reduces the band gap and improves the surface reaction kinetics. Additionally, the HR-TEM results (Fig. 1c & 1e) show that the (220) and (311) planes of Co<sub>3</sub>O<sub>4</sub> are the main planes on the surfaces of nanoparticles. Thus, the (311) surface was used for investigating the influence of Ni-incorporation on the HER and NO<sub>3</sub>RR behavior (Fig. 4c). The desorption energy of adsorbed hydrogen on the Ni-Co<sub>3</sub>O<sub>4</sub> surface (1.02 eV) is higher than that on the Co<sub>3</sub>O<sub>4</sub> surface (0.90 eV) (Fig. 4d), indicating that the Ni-incorporation weakens the Co-O bond, and improves the interaction between the O ion and adsorbed hydrogen, leading to the poor HER performance. The calculated NO<sub>3</sub>RR pathways on the Co<sub>3</sub>O<sub>4</sub> and Ni-Co<sub>3</sub>O<sub>4</sub> surfaces show that NO<sub>3</sub>RR on these surfaces share the same reaction pathway for ammonia production (Fig. 4e). Although the NO<sub>3</sub>RR processes on Co<sub>3</sub>O<sub>4</sub> and Ni-Co<sub>3</sub>O<sub>4</sub> have the same rate-determining step of “\*NO<sub>3</sub>→\*NO<sub>3</sub>H”, the reaction barrier on Ni-Co<sub>3</sub>O<sub>4</sub> (0.63 eV) is lower than that on Co<sub>3</sub>O<sub>4</sub> (0.79 eV) (Fig. 4e). Hence,

the Ni-incorporation not only suppresses the HER process by enhancing the hydrogen adsorption on the surface, but promotes NO<sub>3</sub>RR by reducing the energy barrier for ammonia synthesis, leading to the high selectivity of Co<sub>0.95</sub>Ni<sub>0.05</sub>/Si and Co<sub>0.75</sub>Ni<sub>0.25</sub>/Si.

#### 4. Conclusions

In summary, we propose a strategy to improve the photoelectrochemical nitrate reduction performance of Si-based photoelectrode by photo-assisted electrodeposition of alloy. We find that the performances of photocathodes with Co-rich co-catalysts are better than those with Ni-rich co-catalysts. Especially, Co<sub>0.95</sub>Ni<sub>0.05</sub>/Si exhibits the highest ammonia yield of 2054 µg h<sup>-1</sup> cm<sup>-2</sup> with a superior FE of 98.6% at only -0.1 V vs. RHE, which are much better than those of reported p-NO<sub>3</sub>RR photocathodes. We show that the co-catalyst (Co<sub>0.95</sub>Ni<sub>0.05</sub>) is composed of Ni-incorporated Co<sub>3</sub>O<sub>4</sub> as shell that is the active layer for the nitrate reduction and metallic-Co as core that improves the electron transfer between Si and the active layer. The combined experimental and computational study shows that the inner metallic Co ensures efficient electron transfer and thus high photovoltage, while the Ni-incorporation in Co<sub>3</sub>O<sub>4</sub> improves the reaction kinetics and ammonia selectivity. Our findings may provide an insightful understanding of the photoelectrochemical origin and demonstrate that co-deposition is an effective way to engineer the co-catalyst for Si-based photocathode to enhance the activity and selectivity towards efficient ammonia production by p-NO<sub>3</sub>RR.

#### CRediT authorship contribution statement

**Haoyun Bai:** Writing – review & editing, Data curation, Conceptualization. **Lulu Qiao:** Validation, Investigation, Data curation. **Chunfa Liu:** Writing – review & editing, Validation, Data curation. **Keyu An:** Investigation, Data curation. **Shuangpeng Wang:** Supervision, Project administration, Funding acquisition. **Shengjie Peng:** Supervision, Project administration. **Hui Pan:** Writing – review & editing, Supervision, Project administration, Funding acquisition, Conceptualization. **Shuyang Peng:** Validation, Investigation, Data curation, Conceptualization. **Weng Fai Ip:** Writing – review & editing, Supervision, Project administration, Funding acquisition. **Di Liu:** Writing – review & editing, Writing – original draft, Investigation, Data curation, Conceptualization. **Mingpeng Chen:** Investigation, Data curation. **Kar Wei Ng:** Writing – review & editing, Supervision, Funding acquisition. **Kin Ho Lo:** Supervision, Project administration, Funding acquisition.

#### Declaration of Competing Interest

The authors declare that they have no known competing financial interests or personal relationships that could have appeared to influence the work reported in this paper.

#### Data Availability

Data will be made available on request.

#### Acknowledgements

This work was supported by the Science and Technology Development Fund (FDCT) from Macau SAR (006/2022/ALC, 0111/2022/A2, 0032/2021/ITP, 0050–2023-RIB2, and 0023/2023/AFJ), Multi-Year Research Grants (MYRG2020–00026-FST, MYRG-CRG202200016-ICMS, MYRG-GRG2023–00010-IAPME, and MYRG2022–00026-IAPME) from Research & Development Office at University of Macau, and Shenzhen-Hong Kong-Macao Science and Technology Research Programme (Type C) (SGDX20210823103803017) from Shenzhen. The DFT calculations are performed at High-Performance Computing Cluster (HPCC) of Information, Communication Technology Office (ICTO) at

University of Macau.

#### Appendix A. Supporting information

Supplementary data associated with this article can be found in the online version at doi:10.1016/j.apcatb.2024.123980.

#### References

- [1] B. Zhou, Y. Ma, P. Ou, Z. Ye, X.-Y. Li, S. Vanka, T. Ma, H. Sun, P. Wang, P. Zhou, J. K. Cooper, Y. Xiao, I.A. Navid, J. Pan, J. Song, Z. Mi, Light-driven synthesis of C<sub>2</sub>H<sub>6</sub> from CO<sub>2</sub> and H<sub>2</sub>O on a bimetallic AuIr composite supported on InGaN nanowires, *Nat. Catal.* 6 (11) (2023) 987–995.
- [2] Y. Zhao, B.P. Setzler, J. Wang, J. Nash, T. Wang, B. Xu, Y. Yan, An efficient direct ammonia fuel cell for affordable carbon-neutral transportation, *Joule* 3 (10) (2019) 2472–2484.
- [3] Q. Zhang, D. Liu, Y. Zhang, Z. Guo, M. Chen, Y. Chen, B. Jin, Y. Song, H. Pan, Insight into coupled Ni-Co dual-metal atom catalysts for efficient synergistic electrochemical CO<sub>2</sub> reduction, *J. Energy Chem.* 87 (2023) 509–517.
- [4] Y. Dai, H. Li, C. Wang, W. Xue, M. Zhang, D. Zhao, J. Xue, J. Li, L. Luo, C. Liu, X. Li, P. Cui, Q. Jiang, T. Zheng, S. Gu, Y. Zhang, J. Xiao, C. Xia, J. Zeng, Manipulating local coordination of copper single atom catalyst enables efficient CO<sub>2</sub>-to-CH<sub>4</sub> conversion, *Nat. Commun.* 14 (1) (2023) 3382.
- [5] P.H. van Langevelde, I. Katsounaros, M.T. Koper, Electrocatalytic nitrate reduction for sustainable ammonia production, *Joule* 5 (2) (2021) 290–294.
- [6] F.-Y. Chen, Z.-Y. Wu, S. Gupta, D.J. Rivera, S.V. Lambeets, S. Pecaut, J.Y.T. Kim, P. Zhu, Y.Z. Finfrock, D.M. Meira, G. King, G. Gao, W. Xu, D.A. Cullen, H. Zhou, Y. Han, D.E. Pereea, C.L. Muhiich, H. Wang, Efficient conversion of low-concentration nitrate sources into ammonia on a Ru-dispersed Cu nanowire electrocatalyst, *Nat. Nanotechnol.* 17 (7) (2022) 759–767.
- [7] L. Yue, W. Song, L. Zhang, Y. Luo, Y. Wang, T. Li, B. Ying, S. Sun, D. Zheng, Q. Liu, A. Farouk, M.S. Hamdy, S. Alfaifi, X. Sun, Recent advances in heterogenous electrocatalysts for highly selective nitrite reduction to ammonia under ambient condition, *Small Struct.* (2023) 2300168 (n/a/n.a).
- [8] G. Qing, R. Ghazfar, S.T. Jackowski, F. Habibzadeh, M.M. Ashtiani, C.-P. Chen, M. R., I.I. Smith, T.W. Hamann, Recent advances and challenges of electrocatalytic N<sub>2</sub> reduction to ammonia, *Chem. Rev.* 120 (12) (2020) 5437–5516.
- [9] J. Feng, H. Pan, Electronic state optimization for electrochemical N<sub>2</sub> reduction reaction in aqueous solution, *J. Mater. Chem. A* 8 (28) (2020) 13896–13915.
- [10] J. Liang, Q. Liu, A.A. Alshehri, X. Sun, Recent advances in nanostructured heterogeneous catalysts for N-cycle electrocatalysis, *Nano Res. Energy* 1 (2022) 9120010.
- [11] L. Zhang, J. Liang, Y. Wang, T. Mou, Y. Lin, L. Yue, T. Li, Q. Liu, Y. Luo, N. Li, B. Tang, Y. Liu, S. Gao, A.A. Alshehri, X. Guo, D. Ma, X. Sun, High-performance electrochemical NO reduction into NH<sub>3</sub> by MoS<sub>2</sub> nanosheet, *Angew. Chem. Int. Ed.* 60 (48) (2021) 25263–25268.
- [12] J. Liang, H. Chen, T. Mou, L. Zhang, Y. Lin, L. Yue, Y. Luo, Q. Liu, N. Li, A. A. Alshehri, I. Shakir, P.O. Agboola, Y. Wang, B. Tang, D. Ma, X. Sun, Coupling denitrification and ammonia synthesis via selective electrochemical reduction of nitric oxide over Fe2O3 nanorods, *J. Mater. Chem. A* 10 (12) (2022) 6454–6462.
- [13] D. Liu, H. Ai, W.T. Lou, F. Li, K.H. Lo, S. Wang, H. Pan, Substrate strain engineering: an efficient strategy to enhance the catalytic activity of SACs on waved graphene for e-NRR, *Sustain. Energy Fuels* 4 (7) (2020) 3773–3779.
- [14] L. Zhang, X. Ji, X. Ren, Y. Ma, X. Shi, Z. Tian, A.M. Asiri, L. Chen, B. Tang, X. Sun, Electrochemical ammonia synthesis via nitrogen reduction reaction on a MoS<sub>2</sub> catalyst: theoretical and experimental studies, *Adv. Mater.* 30 (28) (2018) 1800191.
- [15] R. Zhao, H. Xie, L. Chang, X. Zhang, X. Zhu, X. Tong, T. Wang, Y. Luo, P. Wei, Z. Wang, X. Sun, Recent progress in the electrochemical ammonia synthesis under ambient conditions, *EnergyChem* 1 (2) (2019) 100011.
- [16] L. Ouyang, J. Liang, Y. Luo, D. Zheng, S. Sun, Q. Liu, M.S. Hamdy, X. Sun, B. Ying, Recent advances in electrocatalytic ammonia synthesis, *Chin. J. Catal.* 50 (2023) 6–44.
- [17] J. Shao, H. Jing, P. Wei, X. Fu, L. Pang, Y. Song, K. Ye, M. Li, L. Jiang, J. Ma, R. Li, R. Si, Z. Peng, G. Wang, J. Xiao, Electrochemical synthesis of ammonia from nitric oxide using a copper–tin alloy catalyst, *Nat. Energy* 8 (11) (2023) 1273–1283.
- [18] C.H. Wu, C. Liu, D. Su, H.L. Xin, H.-T. Fang, B. Eren, S. Zhang, C.B. Murray, M. B. Salmeron, Bimetallic synergy in cobalt–palladium nanocatalysts for CO oxidation, *Nat. Catal.* 2 (1) (2019) 78–85.
- [19] J. Zheng, Y. Lyu, M. Qiao, J.P. Veder, R.D. Marco, J. Bradley, R. Wang, Y. Li, A. Huang, S.P. Jiang, S. Wang, Tuning the electron localization of gold enables the control of nitrogen-to-ammonia fixation, *Angew. Chem. Int. Ed.* 58 (51) (2019) 18604–18609.
- [20] L. Zhang, J. Liang, Y. Wang, T. Mou, Y. Lin, L. Yue, T. Li, Q. Liu, Y. Luo, N. Li, High-performance electrochemical NO reduction into NH<sub>3</sub> by MoS<sub>2</sub> nanosheet, *Angew. Chem.* 133 (48) (2021) 25467–25472.
- [21] J.M. McEnaney, A.R. Singh, J.A. Schwalbe, J. Kibsgaard, J.C. Lin, M. Cargnello, T. F. Jarillo, J.K. Norskov, Ammonia synthesis from N<sub>2</sub> and H<sub>2</sub>O using a lithium cycling electrification strategy at atmospheric pressure, *Energy Environ. Sci.* 10 (7) (2017) 1621–1630.
- [22] L. Hollevoet, F. Jardali, Y. Gorbanev, J. Creel, A. Bogaerts, J.A. Martens, Towards green ammonia synthesis through plasma-driven nitrogen oxidation and catalytic reduction, *Angew. Chem.* 132 (52) (2020) 24033–24037.

- [23] X. Fan, L. Xie, J. Liang, Y. Ren, L. Zhang, L. Yue, T. Li, Y. Luo, N. Li, B. Tang, Y. Liu, S. Gao, A.A. Alshehri, Q. Liu, Q. Kong, X. Sun, In situ grown Fe<sub>3</sub>O<sub>4</sub> particle on stainless steel: a highly efficient electrocatalyst for nitrate reduction to ammonia, *Nano Res.* **15** (4) (2022) 3050–3055.
- [24] H. Jing, J. Long, H. Li, X. Fu, J. Xiao, Computational insights on potential dependence of electrocatalytic synthesis of ammonia from nitrate, *Chin. J. Catal.* **48** (2023) 205–213.
- [25] D. Liu, L. Qiao, Y. Chen, P. Zhou, J. Feng, C.C. Leong, K.W. Ng, S. Peng, S. Wang, W.F. Ip, H. Pan, Electrocatalytic reduction of nitrate to ammonia on low-cost manganese-incorporated Co<sub>3</sub>O<sub>4</sub> nanotubes, *Appl. Catal. B: Environ.* **324** (2023) 122293.
- [26] D. Liu, L. Qiao, S. Peng, H. Bai, C. Liu, W.F. Ip, K.H. Lo, H. Liu, K.W. Ng, S. Wang, X. Yang, H. Pan, Recent advances in electrocatalysts for efficient nitrate reduction to ammonia, *Adv. Funct. Mater.* (2023) 2303480 (n/a (n/a)).
- [27] Z. Deng, C. Ma, Z. Li, Y. Luo, L. Zhang, S. Sun, Q. Liu, J. Du, Q. Lu, B. Zheng, High-efficiency electrochemical nitrate reduction to ammonia on a Co<sub>3</sub>O<sub>4</sub> nanoarray catalyst with cobalt vacancies, *ACS Appl. Mater. Interfaces* **14** (41) (2022) 46595–46602.
- [28] Y. Zhang, X. Chen, W. Wang, L. Yin, J.C. Crittenden, Electrocatalytic nitrate reduction to ammonia on defective Au1Cu (111) single-atom alloys, *Appl. Catal. B: Environ.* **310** (2022) 121346.
- [29] T. Ren, Z. Duan, H. Wang, H. Yu, K. Deng, Z. Wang, H. Wang, L. Wang, Y. Xu, Electrochemical co-production of ammonia and biodegradable polymer monomer glycolic acid via the co-electrolysis of nitrate wastewater and waste plastic, *ACS Catal.* **13** (15) (2023) 10394–10404.
- [30] Z.-Y. Wu, M. Karamad, X. Yong, Q. Huang, D.A. Cullen, P. Zhu, C. Xia, Q. Xiao, M. Shakouri, F.-Y. Chen, J.Y. Kim, Y. Xia, K. Heck, Y. Hu, M.S. Wong, Q. Li, I. Gates, S. Siahrostami, H. Wang, Electrochemical ammonia synthesis via nitrate reduction on Fe single atom catalyst, *Nat. Commun.* **12** (1) (2021) 2870.
- [31] S. Dong, A. Niu, K. Wang, P. Hu, H. Guo, S. Sun, Y. Luo, Q. Liu, X. Sun, T. Li, Modulation of oxygen vacancy and zero-valent zinc in ZnCr<sub>2</sub>O<sub>4</sub> nanofibers by enriching zinc for efficient nitrate reduction, *Appl. Catal. B: Environ.* **333** (2023) 122772.
- [32] H.E. Kim, J. Kim, E.C. Ra, H. Zhang, Y.J. Jang, J.S. Lee, Photoelectrochemical nitrate reduction to ammonia on ordered silicon nanowire array photocathodes, *Angew. Chem.* **134** (25) (2022) e202204117.
- [33] F. Wang, Q. Ding, J. Ding, Y. Bai, H. Bai, W. Fan, Frustrated Lewis pairs boosting photoelectrochemical nitrate reduction over ZnIn<sub>2</sub>S<sub>4</sub>/BiVO<sub>4</sub> heterostructure, *Chem. Eng. J.* **450** (2022) 138260.
- [34] X. Li, W. Fan, Y. Bai, Y. Liu, F. Wang, H. Bai, W. Shi, Photoelectrochemical reduction of nitrate to ammonia over CuPc/CeO<sub>2</sub> heterostructure: understanding the synergistic effect between oxygen vacancies and Ce sites, *Chem. Eng. J.* **433** (2022) 133225.
- [35] S. Zhou, K. Sun, C.Y. Toe, J. Yin, J. Huang, Y. Zeng, D. Zhang, W. Chen, O. F. Mohammed, X. Hao, Engineering a kesterite-based photocathode for photoelectrochemical ammonia synthesis from NO<sub>x</sub> reduction, *Adv. Mater.* **34** (29) (2022) 2201670.
- [36] C.-H. Chiang, Y.-T. Kao, P.-H. Wu, T.-R. Liu, J.-W. Lin, P.-T. Chen, J.-W. Lin, S.-C. Yang, H.-L. Chen, S.B. Patil, Efficient ammonia photosynthesis from nitrate by graphene/Si Schottky junction integrated with Ni–Fe LDH catalyst, *J. Mater. Chem. A* **11** (21) (2023) 11179–11186.
- [37] F. Wang, Q. Ding, Y. Bai, H. Bai, S. Wang, W. Fan, Fabrication of an amorphous metal oxide/p-BiVO<sub>4</sub> photocathode: understanding the role of entropy for reducing nitrate to ammonia, *Inorg. Chem. Front.* **9** (4) (2022) 805–813.
- [38] J.R. Hemmerling, A. Mathur, S. Linic, Design principles for efficient and stable water splitting photoelectrocatalysts, *Acc. Chem. Res.* **54** (8) (2021) 1992–2002.
- [39] S. Peng, D. Liu, K. An, Z. Ying, M. Chen, J. Feng, K.H. Lo, H. Pan, n-Si/SiO<sub>x</sub>/CoO<sub>x</sub>-Mo photoanode for efficient photoelectrochemical water oxidation, *Small* (2023) 2304376.
- [40] H.-C. Fu, P. Varadhan, C.-H. Lin, J.-H. He, Spontaneous solar water splitting with decoupling of light absorption and electrocatalysis using silicon back-buried junction, *Nat. Commun.* **11** (1) (2020) 3930.
- [41] W.J. Dong, I.A. Navid, Y. Xiao, J.W. Lim, J.-L. Lee, Z. Mi, CuS-decorated GaN nanowires on silicon photocathodes for converting CO<sub>2</sub> mixture Gas to HCOOH, *J. Am. Chem. Soc.* **143** (27) (2021) 10099–10107.
- [42] B. Liu, S. Feng, L. Yang, C. Li, Z. Luo, T. Wang, J. Gong, Bifacial passivation of n-silicon metal-insulator-semiconductor photoelectrodes for efficient oxygen and hydrogen evolution reactions, *Energy Environ. Sci.* **13** (1) (2020) 221–228.
- [43] S. Lee, L. Ji, A.C. De Palma, E.T. Yu, Scalable, highly stable Si-based metal-insulator-semiconductor photoanodes for water oxidation fabricated using thin-film reactions and electrodeposition, *Nat. Commun.* **12** (1) (2021) 3982.
- [44] J. Jack, Z.J. Ren, Metal-insulator-semiconductor (MIS) photoelectrodes: distance improves performance, *Natl. Sci. Rev.* **8** (8) (2021) nwab089.
- [45] H. Hu, M. Tan, L. Liu, Anomalous codeposition mechanism of Co-Ni alloy nanowires, *J. Alloys Compd.* **715** (2017) 384–389.
- [46] A. Karimzadeh, M. Aliofkhazraei, F.C. Walsh, A review of electrodeposited Ni-Co alloy and composite coatings: microstructure, properties and applications, *Surf. Coat. Technol.* **372** (2019) 463–498.
- [47] T.J. Frankcombe, Y. Liu, Interpretation of oxygen 1s X-ray photoelectron spectroscopy of ZnO, *Chem. Mater.* **35** (14) (2023) 5468–5474.
- [48] L. Qiao, D. Liu, A. Zhu, J. Feng, P. Zhou, C. Liu, K.W. Ng, H. Pan, Nickel-facilitated in-situ surface reconstruction on spinel Co<sub>3</sub>O<sub>4</sub> for enhanced electrochemical nitrate reduction to ammonia, *Appl. Catal. B: Environ.* **340** (2024) 123219.
- [49] J. Yang, H. Qi, A. Li, X. Liu, X. Yang, S. Zhang, Q. Zhao, Q. Jiang, Y. Su, L. Zhang, J.-F. Li, Z.-Q. Tian, W. Liu, A. Wang, T. Zhang, Potential-driven restructuring of Cu single atoms to nanoparticles for boosting the electrochemical reduction of nitrate to ammonia, *J. Am. Chem. Soc.* **144** (27) (2022) 12062–12071.
- [50] J.C. Hill, A.T. Landers, J.A. Switzer, An electrodeposited inhomogeneous metal-insulator-semiconductor junction for efficient photoelectrochemical water oxidation, *Nat. Mater.* **14** (11) (2015) 1150–1155.
- [51] F.A. Laskowski, S.Z. Oener, M.R. Nellist, A.M. Gordon, D.C. Bain, J.L. Fehrs, S. W. Boettcher, Nanoscale semiconductor/catalyst interfaces in photoelectrochemistry, *Nat. Mater.* **19** (1) (2020) 69–76.
- [52] A. Hankin, F.E. Bedoya-Lora, J.C. Alexander, A. Regoutz, G.H. Kelsall, Flat band potential determination: avoiding the pitfalls, *J. Mater. Chem. A* **7** (45) (2019) 26162–26176.
- [53] J.M. Gurrentz, M.J. Rose, Non-catalytic benefits of Ni (II) binding to an Si (111)-PNP construct for photoelectrochemical hydrogen evolution reaction: metal ion induced flat band potential modulation, *J. Am. Chem. Soc.* **142** (12) (2020) 5657–5667.